A CASE AGAINST SPINNING PAHS AS THE SOURCE OF THE ANOMALOUS MICROWAVE EMISSION

Brandon S. Hensley[1,2], B. T. Draine[1], and Aaron M. Meisner[3,4]

[1] Department of Astrophysical Sciences, Princeton University, Princeton, NJ 08544, USA; brandon.s.hensley@jpl.nasa.gov
[2] Jet Propulsion Laboratory, California Institute of Technology, 4800 Oak Grove Drive, Pasadena, CA 91109, USA
[3] Berkeley Center for Cosmological Physics, Berkeley, CA 94720, USA
[4] Lawrence Berkeley National Laboratory, Berkeley, CA 94720, USA

ABSTRACT

We employ an all-sky map of the anomalous microwave emission (AME) produced by component separation of the microwave sky to study correlations between the AME and Galactic dust properties. We find that while the AME is highly correlated with all tracers of dust emission, the best predictor of the AME strength is the dust radiance. Fluctuations in the AME intensity per dust radiance are uncorrelated with fluctuations in the emission from polycyclic aromatic hydrocarbons (PAHs), casting doubt on the association between AME and PAHs. The PAH abundance is strongly correlated with the dust optical depth and dust radiance, consistent with PAH destruction in low density regions. We find that the AME intensity increases with increasing radiation field strength, at variance with predictions from the spinning dust hypothesis. Finally, the temperature dependence of the AME per dust radiance disfavors the interpretation of the AME as thermal emission. A reconsideration of other AME carriers, such as ultrasmall silicates, and other emission mechanisms, such as magnetic dipole emission, is warranted.

Key words: dust, extinction – radiation mechanisms: general – radio continuum: ISM

1. INTRODUCTION

High sensitivity, full-sky observations of the far-infrared and microwave sky from *WMAP* and *Planck* have pushed studies of the cosmic microwave background (CMB) to a regime in which contamination from Galactic foregrounds has become a key uncertainty in the analysis. Understanding the physical nature of the foreground components and producing better models of each are essential for mitigating this uncertainty.

The anomalous microwave emission (AME) is perhaps the least well-understood of the foreground components. Discovered as a dust-correlated emission excess peaking near 30 GHz (Kogut et al. 1996; de Oliveira-Costa et al. 1997; Leitch et al. 1997), AME is often ascribed to electric dipole emission from rapidly rotating ultrasmall dust grains (Draine & Lazarian 1998a, 1998b; Hoang et al. 2010; Ysard & Verstraete 2010; Silsbee et al. 2011), i.e., "spinning dust emission." Empirically, this emission component peaks between ~20 and 50 GHz (e.g., Planck Collaboration et al. 2014c) and has an emissivity per H of ~3 × 10^{-18} Jy sr^{-1} cm^2 H^{-1} at 30 GHz (Dobler et al. 2009; Tibbs et al. 2010, 2011; Planck Collaboration et al. 2014c, 2014b). Polycyclic aromatic hydrocarbons (PAHs), which give rise to prominent emission features in the infrared, are considered natural carriers of the AME due to their small size and apparent abundance (Draine & Lazarian 1998a).

Theoretical spinning dust spectral energy distribution (SED) templates based on a PAH size distribution that reproduces the infrared emission features have been successful in fitting observations of the AME both in the Galaxy (Miville-Deschênes et al. 2008; Hoang et al. 2011; Planck Collaboration et al. 2015b) and in the sole extragalactic AME detection in the star-forming galaxy NGC 6946 (Murphy et al. 2010; Scaife et al. 2010; Hensley et al. 2015).

The AME has been observed to correlate well with the PAH emission features in the infrared. Ysard et al. (2010) found that, over the full sky, the AME was more correlated with emission at 12 μm than with 100 μm. Likewise, the AME in the dark cloud LDN 1622 was better correlated with the 12 and 25 μm emission than with either the 60 or 100 μm emission (Casassus et al. 2006). However, studying the AME in a sample of 98 Galactic clouds, the Planck Collaboration et al. (2014c) found no significant differences between the 12, 25, 60, and 100 μm emission in their correlation with the AME. Analysis of both the Perseus molecular cloud (Tibbs et al. 2011) and the HII region RCW175 found no compelling link between the PAH abundance and the AME. Likewise, the link between the AME and PAH abundance determined from dust model fitting has proven tenuous in NGC 6946 (Hensley et al. 2015).

In addition to spinning ultrasmall grains, grains containing ferro- or ferrimagnetic materials are also predicted to radiate strongly in the microwave and may contribute to the AME (Draine & Lazarian 1999; Draine & Hensley 2013). Draine & Lazarian (1999) argued that the spinning dust and magnetic emission mechanisms could be distinguished by observing the AME in dense regions where PAHs would likely be depleted due to coagulation. If the AME per dust mass is constant across both dense and diffuse regions, then spinning dust emission would be disfavored.

In this work, we test the spinning PAH hypothesis using new full-sky observations of the infrared and microwave sky. The Planck Collaboration et al. (2015b) decomposed the *Planck* sky into foreground components making use of both the 9 year *WMAP* data and the Haslam 408 MHz survey. The combination of these data allowed the low-frequency foreground components—primarily synchrotron, free–free, and AME—to be disentangled, producing a full-sky map of the AME.

All-sky *WISE* observations at 12 μm, a tracer of PAH emission, have natural synergy with the AME map, allowing us to test at high significance the link between the AME and PAHs. Additionally, all-sky dust modeling by the Planck Collaboration et al. (2014a) permits deeper exploration into the

dust and environmental parameters that influence the strength of the AME.

This paper is organized as follows: in Section 2 we summarize the data sets used in our analysis; in Section 3 we describe the correlations predicted by our current understanding of the spinning PAH hypothesis; in Section 4 we present the relationships between environmental and dust properties and AME as derived from the data; in Section 5 we discuss the implications of these results on spinning dust theory in particular and AME modeling in general; and we summarize our principal conclusions in Section 6.

2. DATA

2.1. Planck Foreground Separation Maps

Combining full-mission all-sky *Planck* observations (Planck Collaboration et al. 2015a) with the 9 year *WMAP* data (Bennett et al. 2013) and the Haslam 408 MHz survey (Haslam et al. 1982), the Planck Collaboration et al. (2015b) used data from 32 different detectors spanning a range of 408 MHz–857 GHz in frequency to perform foreground component separation within the Bayesian Commander analysis framework (Eriksen et al. 2004, 2006, 2008). They constructed theoretically motivated models for the frequency dependence of each component—including the CMB, synchrotron, free–free, thermal dust, and AME—while minimizing the number of free parameters needed and simultaneously fitting for calibration offsets. Using a Gibbs sampling algorithm, they determined the best-fit values for each model parameter on a pixel-by-pixel basis. We emphasize that this algorithm is not based on spatial templates, but rather parameterized spectral templates which are fit to each pixel independently.

In this work, we focus primarily upon the resulting map of the AME. This component was modeled by the sum of *two* spinning dust spectra with fixed spectral shape as determined by the SpDust code (Ali-Haïmoud et al. 2009; Silsbee et al. 2011), but differing amplitudes and peak frequencies. One of the spectra was required to have a spatially fixed peak frequency, fit to be 33.35 GHz, while the other peak frequency was allowed to freely vary from pixel to pixel. Thus, the data products consist of an amplitude for each AME component, the peak frequency of the spatially varying component, and the uncertainty of each for every pixel on the sky.

To facilitate comparisons with the literature, we calculate the sum of the two components at 30 GHz. We also calculate the uncertainty in this quantity assuming Gaussian errors and ignoring the uncertainty on the peak frequency of both components.

In addition to the AME map, we employ the parameters from the thermal dust fit to compute the 353 GHz dust optical depth τ_{353}. Although this parameter was also an explicit data product of the full-sky modified blackbody fits performed by the Planck Collaboration et al. (2014a), we prefer to use the results from the Planck Collaboration et al. (2015b) study for several reasons. First, the fits were performed on more data and with more detailed treatment of calibration and bandpass uncertainties. Second, the fits were performed at 1° versus 5′ resolution, mitigating the effects of cosmic infrared background anisotropies. Finally, a single-temperature modified blackbody model has been demonstrated to be inadequate to fit the far-IR (FIR) dust emission from *Planck* HFI frequencies to 100 μm (Meisner & Finkbeiner 2015; Planck Collaboration et al.

2015b). Thus, we prefer to use a τ_{353} derived from fits to the Rayleigh–Jeans portion of the dust emission spectrum only. We find τ_{353} derived in this way to be on average 10% lower than that reported by the Planck Collaboration et al. (2014a).

Additionally we employ the parameter maps that characterize the free–free, synchrotron, and CO emission. As free–free and CO emission cannot be fit reliably in regions of low surface brightness, we exclude all pixels with emission measure of 0.1 cm^{-6} pc or less and with no fit CO emission when analyzing the former and latter, respectively.

The Commander parameter maps have a resolution of 1° (FWHM) and are pixellated with HEALPix (Górski et al. 2005) resolution of $N_{side} = 256$. For our analysis, we downgrade these maps to $N_{side} = 128$, corresponding to pixels of about 27.′5 on a side, to critically sample the 1° FWHM.

2.2. Dust Parameter Maps from Modified Blackbody Fitting

A key limitation of the thermal dust fits performed by the Planck Collaboration et al. (2015b) is the omission of any data at higher frequency than the *Planck* 857 GHz band. Without information on the Wien side of the dust emission spectrum, it is difficult to constrain the dust temperature and luminosity.

Thus, we employ the full-sky parameter maps of the Planck Collaboration et al. (2014a), who fit a modified blackbody model of the dust emission to the 2013 *Planck* 857, 545, and 353 GHz data as well as 100 μm data from IRAS. For the latter, they employ both the reprocessed IRIS map (Miville-Deschênes & Lagache 2005) as well as the map of Schlegel et al. (1998). The fits were performed at 5′ resolution and yielded an estimate of τ_{353}, the dust radiance $\mathcal{R} \equiv \int I_\nu^{dust} d\nu$, the dust temperature T_d, and the dust spectral index $\beta \equiv d \ln \tau / d \ln \nu$ for each pixel. We employ $\mathcal{R}$, T_d, and β from these fits in our analysis, but use τ_{353} from the Commander fits as discussed above.

We use the parameter map pixellated with HEALPix resolution of $N_{side} = 2048$, then smooth with a Gaussian beam of FWHM 1° and downgrade the resolution to $N_{side} = 128$.

2.3. WISE 12 μm Map

WISE observed the full sky in four infrared bands—3.4, 4.6, 12, and 22 μm (Wright et al. 2010). The 12 μm channel (*W*3), sensitive from 7 to 17 μm, captures the strongest of the infrared emission features associated with PAHs and thus traces the population of small dust grains. The full-sky *WISE* 12 μm imaging has been reprocessed by Meisner & Finkbeiner (2014) to isolate diffuse emission from Galactic dust at 15″ resolution.

Because interplanetary dust models are insufficiently accurate to remove zodiacal light from the *W*3 data, Meisner & Finkbeiner (2014) adopted a zero level based on the *Planck* 857 GHz map, essentially replacing 12 μm modes on scales larger than 2° with a rescaling of 857 GHz dust emission. Since we wish to study real fluctuations in PAH emission per FIR dust radiance on 1° scales, this zero level procedure has the potential to artificially suppress part of our signal.

Our analysis relies on quantifying the PAH abundance in a given pixel through the ratio of the *W*3 emission to the FIR dust radiance $\mathcal{R}$, a quantity we designate f_{PAH} (see Section 3.2). Computing f_{PAH} via simple division of the Meisner & Finkbeiner (2014) *W*3 map by $\mathcal{R}$ is problematic because this

method is sensitive to the *Planck* 857 GHz based 12 μm large-scale zero level.

We therefore employ an alternative approach to compute f_{PAH}, leveraging the excellent angular resolution of *WISE* and *Planck* to render the large-scale zero level of the $W3$ map irrelevant. Our principal analysis employs $N_{\mathrm{side}} = 128$ HealPix pixels of $\sim0°.5$ on a side. To determine f_{PAH}, we subdivide each of these pixels into approximately 120 subpixels of $2'.5$ on a side and then derive the best-fit correlation slope of $W3$ emission versus $\mathcal{R}$ across the 120 subpixels. To infer the optimal f_{PAH} value within a single HEALPix pixel, we employ the model

$$(\nu I_\nu)_i^{12\,\mu\mathrm{m}} = \mathcal{R}_i \times f_{\mathrm{PAH}} + C, \qquad (1)$$

where, in the ith subpixel, $(\nu I_\nu)_i^{12\,\mu\mathrm{m}}$ is the $W3$ map smoothed to $5'$ resolution and high-pass filtered at $15'$, and $\mathcal{R}_i$ is the *Planck* radiance map (Planck Collaboration et al. 2014a) high-pass filtered at $15'$. The high-pass filtering serves to remove large-scale modes from the comparison, and the offset C is a nuisance parameter. Because linear regression can become sensitive to the choice of fitting methodology in the limit of poor signal-to-noise (see, e.g., Hogg et al. 2010), we restrict analyses of these f_{PAH} correlation slopes to HEALPix pixels with strong linear correlation between $(\nu I_\nu)^{12\,\mu\mathrm{m}}$ and $\mathcal{R}$, using a threshold of Pearson $r > 0.6$. This threshold roughly corresponds to a 10% fractional uncertainty on the inferred f_{PAH}.

The f_{PAH} map derived in this way is qualitatively similar to that obtained by simply dividing the 12 μm map by $\mathcal{R}$, but displays a factor of ~2 broader range of f_{PAH} values. Our basic conclusions are unaffected by the choice of f_{PAH} map and we employ the map obtained with Equation (1) as the default.

Only in the case of Figure 7 do we require a map of the 12 μm emission itself, rather than f_{PAH}. For this purpose, we generated a custom version of the Meisner & Finkbeiner (2014) $W3$ map by replacing only modes larger than $4°.5$ with a rescaling based on the *Planck* 857 GHz emission. This better preserves real fluctuations in 12 μm emission per $\mathcal{R}$ on $\simeq1°$ scales.

Both our final maps of *WISE* 12 μm and f_{PAH} are pixellated with HEALPix resolution of $N_{\mathrm{side}} = 128$.

2.4. IRAS 100 μm Map

As our analysis is performed on scales of $\simeq1°$, we follow the Planck Collaboration et al. (2014a) in employing the IRAS 100 μm map of Schlegel et al. (1998). We do not, however, employ the reprocessed IRIS maps (Miville-Deschênes & Lagache 2005) on small scales as was done by the Planck Collaboration et al. (2014a). We note that using the IRIS map instead in our analysis somewhat degrades the tightness of the correlation between the 100 μm emission and the AME, particularly in regions of low surface brightness. The effect is small and has limited impact on our conclusions.

We smooth the IRAS 100 μm map of Schlegel et al. (1998) to a FWHM of $1°$ and pixellate with $N_{\mathrm{side}} = 128$.

2.5. Masks

Zodiacal light in the ecliptic plane can dominate the signal from PAH emission at 12 μm even on small angular scales, thereby biasing our primary PAH tracer. We therefore exclude all pixels within five degrees of the ecliptic plane (8.7% of the sky) to mitigate this effect.

Likewise, artifacts from moon contamination are also present in the 12 μm map. We therefore mask all pixels flagged for moon contamination by Meisner & Finkbeiner (2014), totaling 16% of the sky. Since our analysis requires that both $\mathcal{R}$ and $I_\nu^{12\,\mu\mathrm{m}}$ measure true dust emission, and since these quantities will closely correlate when they do, we require every pixel in our analysis to have a Pearson $r > 0.6$ between $\mathcal{R}$ and $I_\nu^{12\,\mu\mathrm{m}}$ across its $2'.5$ subpixels as described in Section 2.3. This cut alone eliminates 42% of the sky, mostly at low surface brightness and high Galactic latitude where *WISE* lacks sufficient sensitivity to measure diffuse dust emission.

Although nominally a full-sky mission, IRAS did not have 100% sky coverage. We therefore mask the regions IRAS did not observe (Wheelock et al. 1994), totaling 2% of the sky, as the 100 μm emission in these regions estimated using lower resolution DIRBE data (Schlegel et al. 1998) may not be reliable.

To mitigate the effects of point sources, we employ the *Planck* point source masks in intensity at each HFI[5] and LFI[6] band (Planck Collaboration et al. 2015a). These masks eliminate point sources with signal-to-noise greater than 5 at resolution $N_{\mathrm{side}} = 2048$. We downgrade these masks to $N_{\mathrm{side}} = 128$ by rejecting any pixel containing a point source, resulting in 39% of the sky being masked due to point sources.

Finally, we use the *Planck* Galactic plane mask covering 1% of the sky based on the 353 GHz HFI data[7] (Planck Collaboration et al. 2015a). This eliminates the regions in the Galactic plane with the most complicated and highest intensity emission and where the relatively simple foreground models are most likely to break down.

After applying the masks described above, 51,579 pixels covering 26% of the sky remain. The total mask is illustrated in Figure 1 on the full-sky $\mathcal{R}$ map. This combination of masks is used in all analyses, although we discuss the sensitivity of our results to various additional masking (e.g., masking the Galactic plane) in Section 4.6.

3. TESTS OF AME THEORY

3.1. AME Theory

The AME has been suggested to be electric dipole emission from ultrasmall, rapidly rotating grains that have been torqued up through interactions with both the gas and radiation field (Draine & Lazarian 1998b; Hoang et al. 2010; Ysard & Verstraete 2010; Silsbee et al. 2011). The observed peak frequency of the emission requires that the grains be small (radius $a \lesssim 10$ Å), leading to a natural association with the PAHs that produce emission features in the infrared.

If so, we might expect a linear relation between the total PAH surface density Σ_{PAH} and the AME intensity. Adopting an empirical 30 GHz spinning dust emissivity of 3×10^{-18} Jy sr^{-1} cm^2 H^{-1}, and assuming this corresponds to typical Galactic values of $M_d/M_H = 0.01$ and $\Sigma_{\mathrm{PAH}}/\Sigma_d = 0.046$

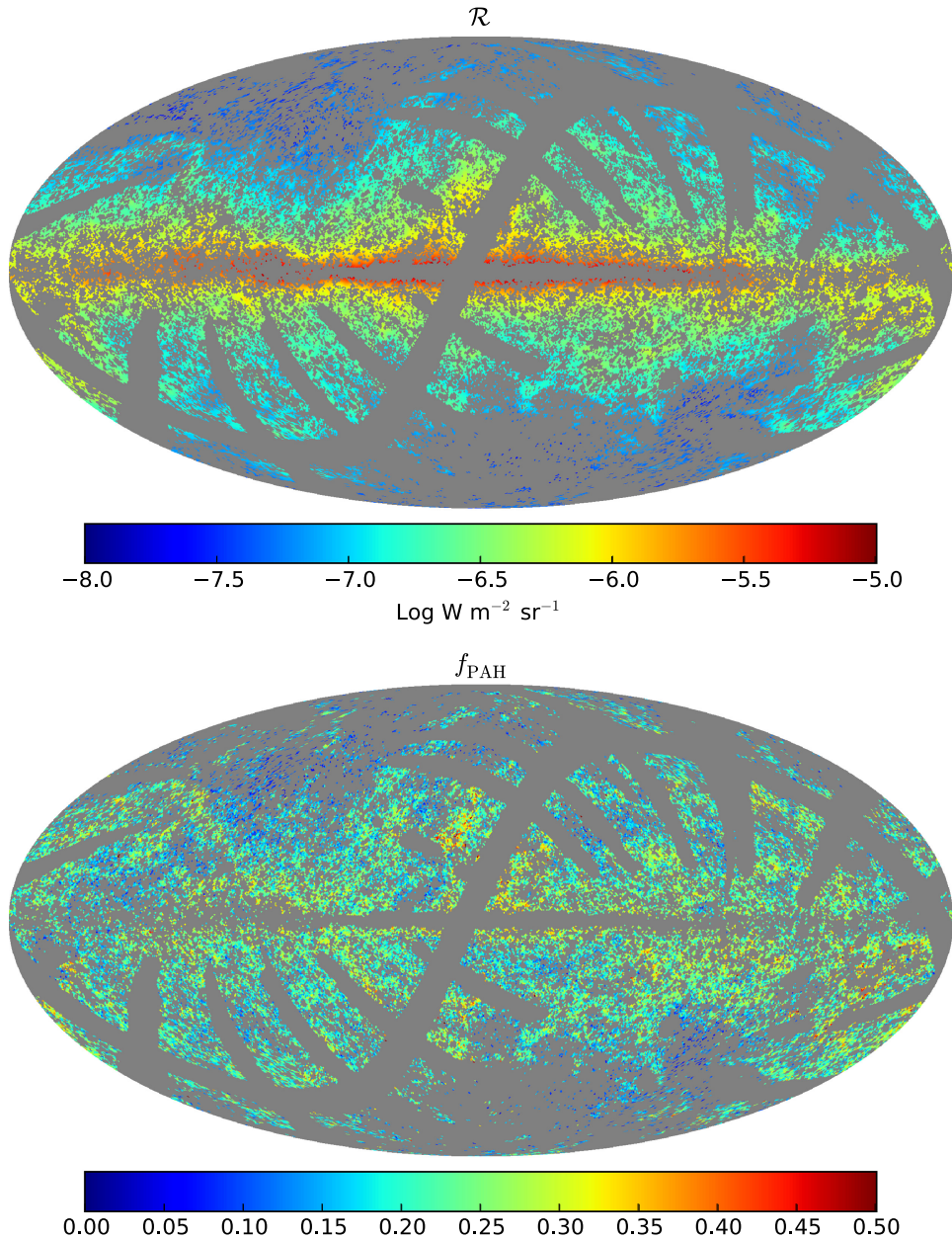$$\mathcal{R}$$

$$f_{\mathrm{PAH}}$$

Figure 1. Top: the Mollweide projection full-sky map of $\mathcal{R}$ as derived by the Planck Collaboration et al. (2014a) with the mask described in Section 2.5 overlaid in gray. The unmasked area comprises 26% of the sky. Bottom: the full-sky map of $f_{\mathrm{PAH}} \equiv (\nu I_\nu)^{12\,\mu\mathrm{m}}/\mathcal{R}$ with the same mask overlaid.

(Draine & Li 2007), we would expect

$$I_{\nu,30\,\mathrm{GHz}}^{\mathrm{AME}} = 0.8 \left(\frac{\Sigma_{\mathrm{PAH}}}{M_\odot \, \mathrm{kpc}^{-2}} \right) \mathrm{Jy\ sr^{-1}}. \qquad (2)$$

In the context of the spinning dust model, environmental factors can influence both the peak frequency of the emission and the emissivity itself. The importance of collisions with ions depends on the fractional ionization and the charge state of the ultrasmall grains. In regions with very intense radiation fields, drag forces from IR photon emission become important. Damping by the rotational emission generally causes the ultrasmall grains to have sub-LTE rotation rates.

The electric dipole moment distribution of the dust population will also strongly influence the emissivity, although we have no a priori estimates of the systematic variations of this quantity from one region to another.

We expect spinning dust emission to be relatively insensitive to the strength of the radiation field, which is an important source of excitation only in fairly extreme environments such as reflection nebulae and photo-dissociation regions. However, the emissivity per unit gas mass should increase with increasing local gas density, which may correlate with the radiation field strength.

The impact of these factors on the 30 GHz AME flux density was estimated by Draine & Lazarian (1998b) to be only about a factor of two between the cold neutral medium, warm neutral medium, and warm ionized medium (WIM) environments. In our study, these effects are mitigated by the low angular resolution of the maps, which are likely to be sampling dust emission from different environments within each pixel.

These caveats notwithstanding, the spinning PAH model for the AME predicts:

1. A linear correlation of the PAH surface density and the AME flux density at 30 GHz.
2. Relatively constant AME per PAH surface density over a range of radiation field strengths.

3.2. Data Model

τ_{353} is equal to the product of the dust mass column density and the dust opacity at 353 GHz. Because dust grains are much smaller than the wavelength of light at this frequency, the dust opacity is insensitive to the size distribution of the grains and τ_{353} is thus a reliable indicator of the total dust column density. There is evidence, however, that the dust optical properties change somewhat in different environments (Planck Collaboration et al. 2014d).

The dust radiance $\mathcal{R}$ is the frequency-integrated dust intensity. $\mathcal{R}$ is estimated using the best-fit single-temperature modified blackbody with $\tau_\nu \propto \nu^\beta$, and is a tracer of both the dust column density and the strength of the radiation field heating the dust.

Finally, the 12 μm flux density is effectively a measure of the total power emitted by PAHs, i.e., the starlight power absorbed by PAHs. Thus, the ratio of the 12 μm emission to the dust radiance is a proxy for the fraction of dust in PAHs (see Equation (1)). The product $f_{\mathrm{PAH}} \tau_{353}$ is then a proxy for the PAH column density. It is this quantity which the spinning dust model predicts to be the most accurate predictor of the strength of the AME.

We assume that τ_{353}, $f_{\mathrm{PAH}} \tau_{353}$, $\mathcal{R}$, $I_\nu^{12\,\mu\mathrm{m}}$, and $I_\nu^{100\,\mu\mathrm{m}}$ correlate with the AME intensity in a linear way, i.e., for each pixel i and each observable A_i, the AME intensity in that pixel is given simply by $\alpha_i A_i$ where α_i is a constant to be determined.

To identify the physical quantity which is the best predictor of the AME intensity, we wish to quantify the intrinsic dispersion in α_i across all pixels. We assume that each pixel samples a Gaussian distribution with mean α and standard deviation σ_α.

The likelihood of this model given the data over all pixels is:

$$\mathcal{L} \propto \prod_i \frac{1}{\sqrt{\sigma_{I,i}^2 + (A_i \sigma_\alpha)^2}} \times \exp\left[\frac{-(I_{\nu,30\,\mathrm{GHz},i}^{\mathrm{AME}} - \alpha A_i)^2}{\sigma_{I,i}^2 + (A_i \sigma_\alpha)^2} \right],$$
(3)

where $\sigma_{I,i}$ is the uncertainty on $I_{\nu,30\,\mathrm{GHz},i}^{\mathrm{AME}}$. We thus seek the maximum likelihood values of α and σ_α for each observable A. In practice, we employ the emcee Markov chain Monte Carlo code (Foreman-Mackey et al. 2013) to derive the best-fit values and confidence intervals for each parameter assuming uninformative priors.

If there are zero point errors in any of the maps used in this analysis, then $I_{\nu,30\,\mathrm{GHz}}^{\mathrm{AME}} = \alpha A + b$ is a more appropriate functional form for the relationship, where b is a parameter to be fit. We find that the introduction of an intercept has little impact on the results, such as the ordering of the σ_α/α, or the value of α.

3.3. Model Caveats

The principal conclusions of this work derive from correlational analysis on the observables described in Sections 2 and 3.2. As such, our conclusions are sensitive to the fidelity with which these observables have been determined, including any spurious correlations induced between observables during fitting. We give an extended discussion of these issues in Section 5, but briefly summarize a few key caveats here.

As we are primarily interested in the link between PAHs and the AME, our measures of PAH emission and AME need to be robust. That we see evidence of PAH destruction in the diffuse ISM (Section 4.1) and the expected trends with Galactic latitude (Section 4.6) gives us confidence in the reliability of our f_{PAH} measurement. Likewise, the remarkable linear correlation of I_ν^{AME} with $\mathcal{R}$, which emerged from an AME fit that did not depend on dust templates, attests to the reliability of the Commander AME maps.

The Commander AME maps were derived from a simultaneous fit involving the AME and thermal dust emission, plausibly leading to co-correlations (or the reduction of existing correlations) between the AME and thermal dust properties induced by the fitting procedure alone. We expect this to be largely mitigated by the fact that the thermal dust properties are primarily dictated by the high-frequency *Planck* data points ($\gtrsim$353 GHz), while the AME fit is sensitive only to the low-frequency data points ($\lesssim$70 GHz). Subsequent foreground component maps resulting from upgraded techniques and new data sets will be invaluable for testing the conclusions we present here.

Finally, as we discuss in Section 3.1, there are theoretical reasons within the spinning PAH paradigm to expect PAH emission and AME not to vary in a one-to-one way due to differences in local environment. We have performed our analysis holding various dust properties fixed, which controls to an extent for these environmental variations, and found no change in the results (Section 5). Nevertheless, it remains possible in the face of the non-correlations presented in this work that PAHs are still responsible for the AME, but that the correlation has somehow been erased by these secondary effects. Detailed theoretical modeling of the AME, thermal dust emission, and the environmental conditions affecting both would be needed to assess the viability of masking correlations between AME and the 12 μm PAH emission within the spinning PAH paradigm.

4. RESULTS

4.1. Correlation with PAH Abundance

We test the predictions of the spinning PAH hypothesis laid out in Section 3.1 by relating the observational data to physical properties of the dust through the model described in Section 3.2.

In Figure 2 we plot the AME flux density at 30 GHz against τ_{353}, $f_{\mathrm{PAH}} \tau_{353}$, the dust radiance $\mathcal{R}$, and the 100 μm flux density $I_\nu^{100\,\mu\mathrm{m}}$. All four correlate highly with AME as expected, and we present the fit slope of the relation with each in Table 1. The tightness of each correlation is indicated by σ_α/α, with $\mathcal{R}$ having the tightest correlation (see Figure 2(c)). In Figure 2, we also note the χ_{red}^2, computed assuming errors on I_ν^{AME} only, as an indicator of the relative goodness of the fits. We caution against overinterpretation of the $\Delta\chi^2 s$ due to both the expected intrinsic scatter and the inability of the errors to capture how well (or how poorly) the Commander fits represent the true AME signal at 30 GHz.

If the AME arises from spinning PAHs, we would expect the emission to correlate better with $f_{\mathrm{PAH}} \tau_{353}$ than τ_{353}. While it is clear that both are good tracers of AME, $f_{\mathrm{PAH}} \tau_{353}$ has a *larger*
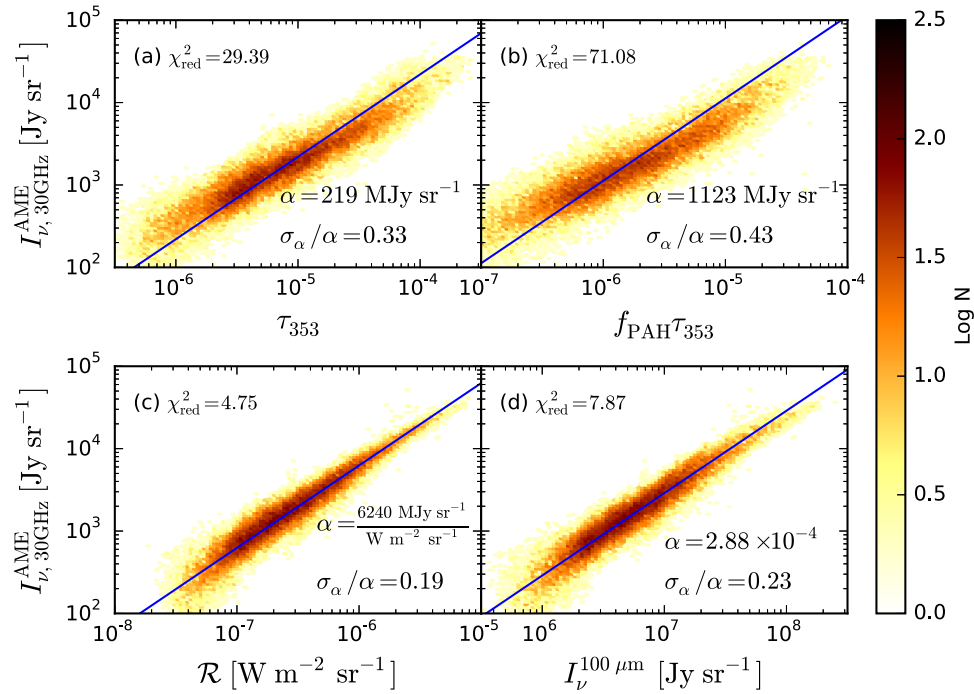
Figure 2. 30 GHz AME intensity is plotted against (a) τ_{353}, (b) $f_{PAH}\tau_{353}$, (c) $\mathcal{R}$, and (d) $I_{\nu}^{100\,\mu m}$. We divide the plot area into hexagons of equal area in log-space and color each according to the number of pixels that fall within that hexagon. Each panel has the same logarithmic area allowing for straightforward comparisons between panels. In doing this, we have restricted the range of each plot to exclude some outlying points. In each panel we also plot (solid blue) the line with slope equal to the best-fit value of α. All four quantities are excellent tracers of the AME, but it is clear that $\mathcal{R}$ traces the AME with the greatest fidelity and least dispersion.

Table 1
Correlation Analysis $I_{\nu,30\,GHz}^{AME} = \alpha A$

A	$\alpha \pm \sigma_\alpha$	σ_α/α	$\sigma_A/A\,(0.2)$
$\mathcal{R}$	$\frac{6240 \pm 1210}{W\,m^{-2}\,sr^{-1}}$ MJy sr^{-1}	0.19	0.01
$I_{\nu}^{12\,\mu m}$	$(7.48 \pm 1.66) \times 10^{-3}$	0.22	0.09
$I_{\nu}^{100\,\mu m}$	$(2.88 \pm 0.65) \times 10^{-4}$	0.23	0.10
τ_{353}	219 ± 72 MJy sr^{-1}	0.33	0.27
$f_{PAH}\,\tau_{353}$	1123 ± 487 MJy sr^{-1}	0.43	0.39

Note. α and σ_α are the best-fit values obtained from Equation (3) for each observable A such that $I_{\nu,30\,GHz}^{AME} = \alpha A$. The formal uncertainties on α and σ_α are less than the quoted accuracy in the table, generally of order 0.1%. $\sigma_A/A\,(0.2)$ denotes the value of σ_A/A such that $\sigma_\alpha/\alpha = 0.2$, indicating the level of observational uncertainty needed in A to produce a relationship with $I_{\nu,30\,GHz}^{AME}$ comparably tight as that observed with $\mathcal{R}$.

dispersion about the best-fit relation than τ_{353}. Maximizing Equation (3), $A = \tau_{353}$ yields a relation with $\sigma_\alpha/\alpha = 0.33$ while $A = f_{PAH}\,\tau_{353}$ yields $\sigma_\alpha/\alpha = 0.43$ (see Table 1). Thus, f_{PAH} does not appear to contain additional information about the strength of the AME not already present in τ_{353}.

The spinning PAH model predicts that variations in the AME intensity per unit dust mass should arise from variations in the abundance of small grains. Therefore, as a second test of the link between the AME and PAHs, we look for correlations between f_{PAH} and the AME per τ_{353}.

In Figure 3(a) we plot the AME intensity normalized by $\alpha\tau_{353}$ against f_{PAH}, but we find no evidence for the expected positive correlation. We quantify this with the Spearman rank correlation coefficient r_s which, unlike the Pearson correlation coefficient, does not assume a functional form for the relationship between the two variables. We find $r_s = -0.15$, suggesting *anti*-correlation. Formally, this and most of the

correlation coefficients quoted in this work are statistically significant due to the large number of data points under consideration. As we are interested in testing whether PAH emission is a *predictor* of AME, we focus on the derived value of r_s, with values close to zero indicating a "weak" correlation and values close to 1 or -1 indicating a "strong" correlation or anti-correlation, respectively.

Quantifying the correlation between f_{PAH} and the AME intensity normalized instead by $\alpha\mathcal{R}$ (see Figure 3(b)) yields $r_s = -0.02$, suggesting that f_{PAH} carries essentially no information on the AME intensity not already present in the dust radiance.

We note that f_{PAH} is itself correlated with both τ_{353} and $\mathcal{R}$ as demonstrated in Figure 4. f_{PAH} (measured on $\sim1°$ scales) varies from ~0.15 to 0.30 over most of the unmasked sky, so that variations in the PAH abundance might have been expected to account for a factor of ~1.5 dispersion in AME intensity per dust mass. It is therefore striking that we detect no correlation of AME/$\mathcal{R}$ with f_{PAH}.

The observed correlation between f_{PAH} and τ_{353} is evidence for PAH destruction in the diffuse ISM (low τ_{353}). Depletion of PAHs by a factor of ~3 to suppress photoelectric heating in the WIM has been invoked to explain high ratios of Hα to free–free emission (Dong & Draine 2011) and is roughly consistent with the range of f_{PAH} we observe.

A study of the Hα-correlated AME by Dobler et al. (2009) found the AME to be a factor of ~3 less intense than the amplitude calculated by Draine & Lazarian (1998a, 1998b) and suggested that this discrepancy was due to PAH depletion in the WIM. However, subsequent studies have suggested an AME amplitude a factor of ~3 lower than the earlier estimates even in Galactic clouds (Tibbs et al. 2010, 2011; Planck Collaboration et al. 2014b, 2014c). Thus, the results of Dobler et al. (2009) indicate instead a robustness of the AME strength
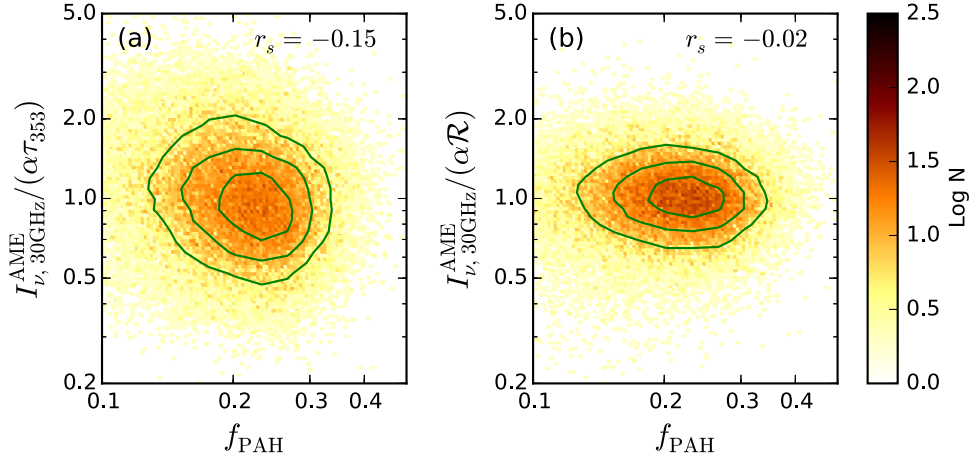
Figure 3. f_{PAH} is plotted against the AME intensity normalized by (a) $\alpha\tau_{353}$ and (b) $\alpha\mathcal{R}$. Here and in subsequent plots, the isodensity contours corresponding to 25%, 50%, and 75% of the pixels enclosed are plotted in green. There is no apparent correlation between f_{PAH} and the AME, at variance with the spinning PAH hypothesis.
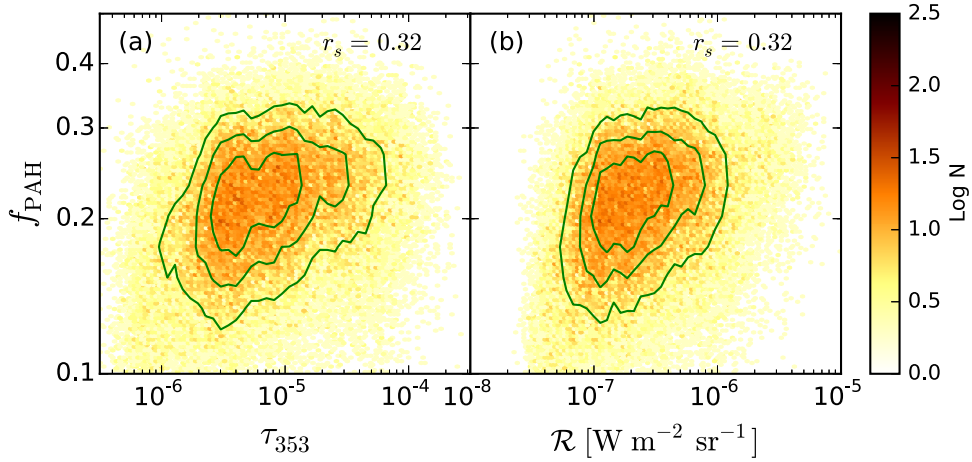

Figure 4. Plotting f_{PAH} against both (a) τ_{353} and (b) $\mathcal{R}$, it is clear that a positive correlation is present with both, consistent with depletion of PAHs in the diffuse ISM. The majority of the pixels have $0.15 < f_{\mathrm{PAH}} < 0.30$, suggesting that fluctuations in PAH abundance could account for a scatter of a factor of at most ~1.5 in AME intensity unit per dust mass.
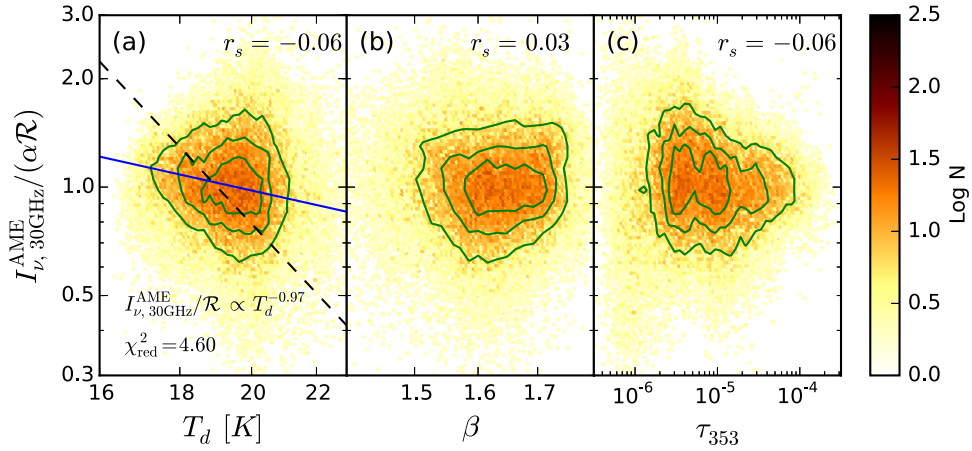

Figure 5. 30 GHz AME intensity normalized by $\alpha\mathcal{R}$ is plotted against (a) T_{d} and (b) β determined by modified blackbody fits to the dust SED (Planck Collaboration et al. 2014a), and against τ_{353} determined from component separation (Planck Collaboration et al. 2015b) in panel (c). Since PAHs are depleted in dense regions, the spinning PAH hypothesis predicts that the AME per $\mathcal{R}$ should be smaller in denser regions. These regions are likely to have more cold dust and thus a smaller β, but no correlation is observed between β or τ_{353} and the AME intensity per $\mathcal{R}$. The data do suggest a possible correlation with T_{d}. We find a best-fit power-law of $T_{\mathrm{d}}^{-0.97}$ (blue solid) and plot also the best-fit relation assuming the AME is thermal emission with $\tau_{30} \propto \tau_{353}$, i.e., $I_\nu^{\mathrm{AME}} \propto \tau_{353}T_{\mathrm{d}}$, hence $I_\nu^{\mathrm{AME}}/R \propto T_{\mathrm{d}}^{-4.65}$ (black dashed). The latter relationship is disfavored relative to the former ($\chi_{\mathrm{red}}^2 = 10.2$ vs. 4.6). Finally, we note that our conclusions are unchanged when we redo this analysis using T_{d} and β determined by Planck Collaboration et al. (2015b).

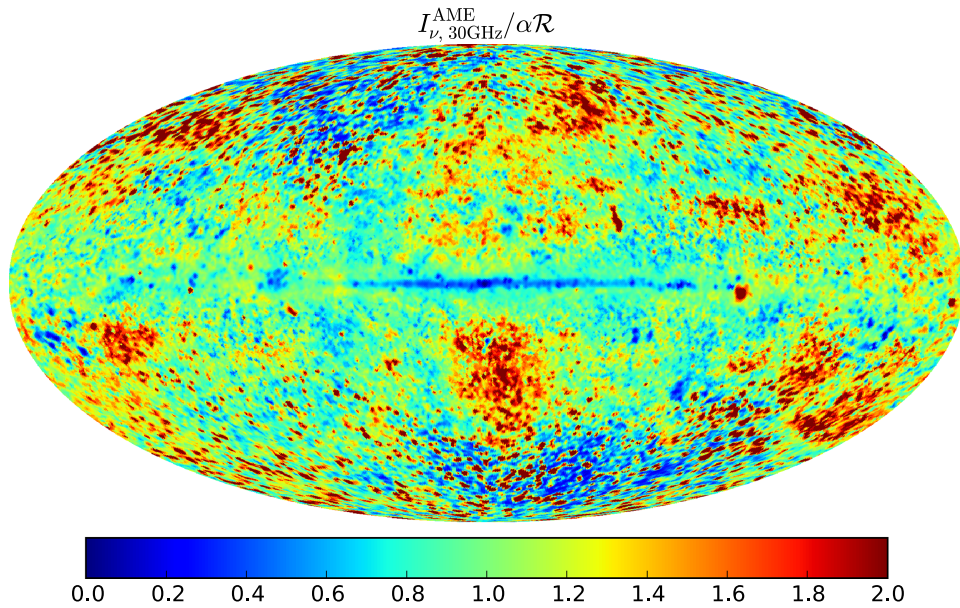$$I_{\nu,\,30\mathrm{GHz}}^{\mathrm{AME}}/\alpha\mathcal{R}$$

Figure 6. Mollweide projection full-sky map of the 30 GHz AME intensity normalized by $\alpha\mathcal{R}$. Although some large-scale features associated with strong synchrotron emission are present, overall the map has little correlation with the synchrotron intensity ($r_s = 0.11$).

across environments and, together with our results, further evidence that the AME is not associated with PAHs.

The correlation between f_{PAH} and τ_{353} also sheds light on the apparent negative correlation observed between f_{PAH} and $I_\nu^{\mathrm{AME}}/\tau_{353}$ in Figure 3(a). Figures 2(a) and 5(c) demonstrate that $\alpha\tau_{353}$ tends to underpredict the true AME intensity at low values of τ_{353} and to overpredict at high values. Since f_{PAH} is positively correlated with τ_{353}, it is not surprising that assuming a linear relationship between the AME and $f_{\mathrm{PAH}}\tau_{353}$ only exacerbates those discrepancies.

4.2. Correlation with the Radiation Field

Figure 2 and Table 1 also indicate the surprising result that the AME is more tightly correlated with $\mathcal{R}$ than τ_{353}. We would expect $\mathcal{R}$ and τ_{353} to be related through the strength of the radiation field—a fixed quantity of dust will radiate more when exposed to more radiation. The most straightforward conclusion is that the AME is enhanced by a stronger radiation field, which runs counter to the predictions of the spinning dust hypothesis (Ali-Haïmoud et al. 2009; Ysard & Verstraete 2010).

A positive correlation between the radiation field strength and the AME intensity has been noted in both the Perseus molecular cloud (Tibbs et al. 2011) and the H II region RCW175 (Tibbs et al. 2012a). This trend was also noted by the Planck Collaboration et al. (2014c), who attribute the correlation to a positive correlation between the radiation field and the local gas density.

The relationship between the AME/$\mathcal{R}$ and T_d, illustrated in 5(a), is best fit by a power-law of index -0.97. If the AME were thermal emission in the Rayleigh–Jeans limit, we would expect I_ν^{AME} to scale linearly with T_d, i.e., $I_{\nu,30\,\mathrm{GHz}}^{\mathrm{AME}} \propto \tau_{30} T_d$. Since $\mathcal{R} \propto T_d^{4+\beta}$ if $\tau_\nu \propto \nu^\beta$, $I_\nu^{\mathrm{AME}}/\mathcal{R}$ should therefore scale as $T_d^{-\beta-3} \approx T_d^{-4.65}$ if the AME is thermal emission and $\beta \approx 1.65$. Fitting the data with a power $T_d^{-4.65}$ yields a substantially worse χ_{red}^2 (10.2 versus 4.6). The data suggest then that the AME is
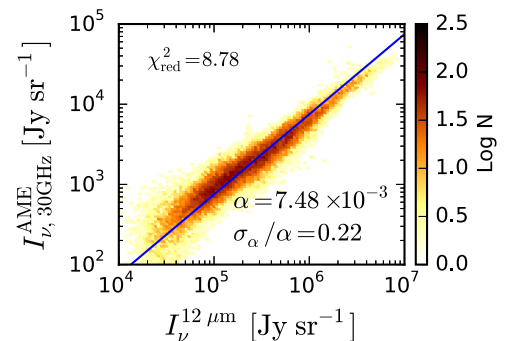

Figure 7. As in each panel of Figure 2, we plot the *WISE* 12 μm intensity against the 30 GHz AME intensity. The correlation is comparably tight as observed with $\mathcal{R}$.

non-thermal emission, unless the dust opacity at 30 GHz has a steep temperature dependence (e.g., $\tau_{30}/\tau_{353} \propto T_d^{3.7}$, where τ_{30} is the dust optical depth at 30 GHz.). We caution that systematic effects arising from fitting a single-T_d modified blackbody to the thermal dust emission may also alter the correlation with T_d and we thus cannot rule out a thermal emission mechanism completely based upon these data alone.

If the fit AME component is contaminated with emission from other low-frequency foregrounds, then this may also induce correlations with T_d. Indeed, Figure 6 reveals some coherent large-scale structures in the map of AME/$\mathcal{R}$ that are likely related to strong synchrotron emission (see Planck Collaboration et al. 2015b, Figure 46) and perhaps the *Fermi* bubbles (Su et al. 2010). We discuss this possibility further in Section 5, although aside from a few clear structures, contamination appears to be minimal.

For pixels containing regions with both high and low radiation intensities, fitting the $\lambda \geqslant 100\,\mu$m emission by a single-temperature modified blackbody will lead to systematic errors, tending to overestimate T_d and underestimate both β and τ_{353}. Thus, if the correlation between the AME and the dust
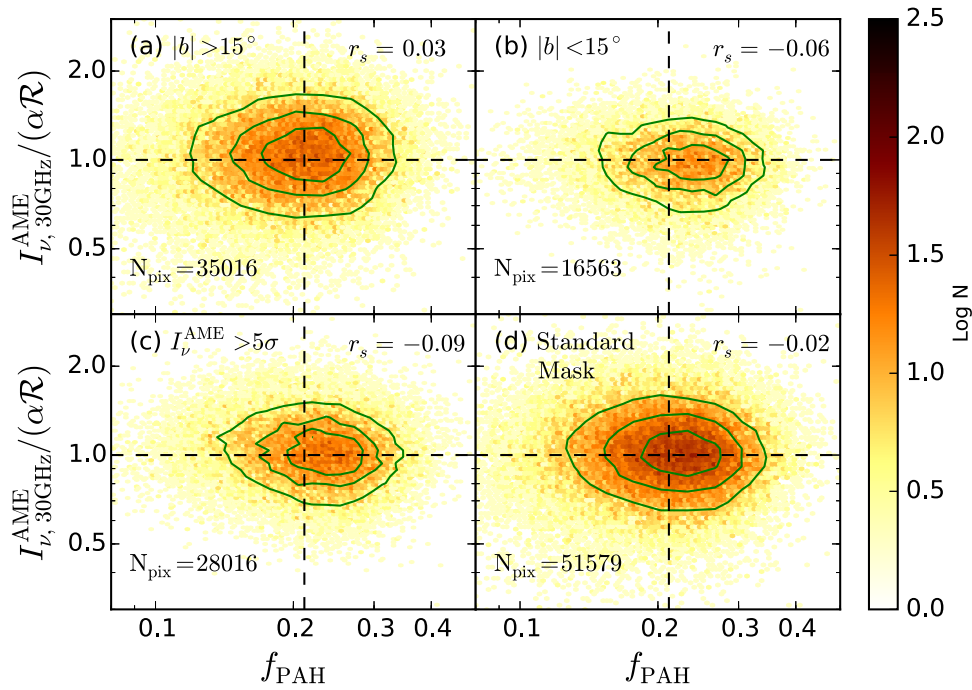
Figure 8. As in Figure 3, f_{PAH} is plotted against the 30 GHz AME intensity normalized by $\alpha\mathcal{R}$. We examine four different masks: (a) considering only higher Galactic latitudes $|b| > 15°$, (b) considering only lower Galactic latitudes $|b| < 15°$, (c) considering only pixels in which at least one AME component was significant at $>5\sigma$, and (d) using the standard mask only. For reference, the dashed lines mark the median values in the standard mask. In all cases, there is no evidence for positive correlation between the AME and f_{PAH}.

radiance is driven by the correlation between the radiation field intensity and the local gas density, we might expect the AME per $\mathcal{R}$ to correlate with β. We find no evidence for such a correlation (see Figure 5(b)).

4.3. Correlation with $I_\nu^{100\,\mu\mathrm{m}}$

The ratio of $I_{\nu,30\,\mathrm{GHz}}^{\mathrm{AME}}$ to $I_\nu^{100\,\mu\mathrm{m}}$ is often quoted in the literature. We obtain a value of $(2.88 \pm 0.65) \times 10^{-4}$ (see Table 1), consistent with other determinations. For instance, performing component separation on *WMAP* observations at intermediate Galactic latitudes, Davies et al. (2006) derived a ratio of 3×10^{-4}. Alves et al. (2010) likewise find a ratio of 3×10^{-4} combining observations of radio recombination lines in the Galactic plane with *WMAP* data. Studying HII regions in the Galactic plane with the Very Small Array at 33 GHz, Todorović et al. (2010) find a ratio of 1×10^{-4}. Analyzing a sample of 98 Galactic clouds with *Planck* observations, the Planck Collaboration et al. (2014c) derived a ratio of 2.5×10^{-4}. Thus, the AME component identified by the Planck Collaboration et al. (2015b) has a strength relative to the 100 μm dust emission in good agreement with what has been observed in other studies.

However, as discussed in detail by Tibbs et al. (2012b), this ratio is subject to significant variability. While the 100 μm emission is a reasonable proxy for the total dust luminosity, its sensitivity to the dust temperature introduces significant nonlinearities in the relationship. This effect is evident at particularly low and high values of $I_\nu^{100\,\mu\mathrm{m}}$ in Figure 2(d) as evidenced by the somewhat nonlinear shape of the scatter plot. As expected, the tightness of the correlation between the AME and 100 μm increases when the analysis is restricted to a set of pixels with similar T_d.

4.4. Correlation with $I_\nu^{12\,\mu\mathrm{m}}$

Finally, we find that the 12 μm emission is also tightly correlated with the AME with dispersion only slightly less than that of $\mathcal{R}$ a shown in Figure 7. While it is tempting to read this as a vindication of the spinning PAH model, the foregoing analysis suggests that this tight correlation is merely the product of the 12 μm emission being an excellent tracer of both the dust column and the radiation field strength. f_{PAH}, i.e., the 12 μm emission per unit $\mathcal{R}$, does not correlate with the AME intensity (see Figures 3(b) and 8).

Thus, while the PAH emission is an excellent predictor of the AME strength, this appears to be by virtue of being an excellent predictor of the dust radiance rather than the result of an inherent link between the AME and PAHs.

4.5. Emission from Magnetic Dust

If the AME is not spinning PAHs, could it be emission from magnetic grains? Draine & Lazarian (1999) predicted that, unlike spinning PAH emission, magnetic dust emission would be equally strong per dust mass in both dense and diffuse regions. Since the dust in dense regions will be cooler than that in diffuse regions, pixels with significant dust emission from both diffuse and dense regions will have broader SEDs and thus are fitted by smaller values of β relative to diffuse regions when fitting the SED with a modified single-T_d blackbody. Thus, the AME per dust mass is predicted to be *negatively* correlated with β in the spinning PAH model and uncorrelated in the magnetic dust model. In Figure 5(b) we demonstrate that AME/$\mathcal{R}$ and β are largely uncorrelated ($r_\mathrm{s} = 0.03$). However, magnetic grains should emit thermally (Draine & Hensley 2013), whereas the relationship derived above between $I_\nu^{\mathrm{AME}}/\mathcal{R}$ and T_d favors a non-thermal emission mechanism. In addition, thermal emission from magnetic dust seems likely

to be polarized (Draine & Hensley 2013) whereas observations find the AME to be minimally polarized (see Section 5 for further discussion of polarization observations).

4.6. Dependence on Masks

The lack of correlation between f_{PAH} and the AME intensity per τ_{353} or $\mathcal{R}$ is a potentially serious problem for the spinning PAH hypothesis. We thus test the sensitivity of this result to the region of the Galaxy examined. In Figure 8, we perform the same analysis as in Figure 3(b) and quantify the degree of correlation with the Spearman correlation coefficient r_s.

Starting with the $N = 51,579$ pixels remaining unmasked following the cuts discussed in Section 2.5, in Figure 8(a) we consider only the pixels with Galactic latitude $|b| > 15°$. The behavior very much mimics that observed in Figure 3(b), with no compelling evidence of a correlation. In Figure 8(b), we examine pixels with $|b| < 15°$. These pixels have more PAH emission per dust radiance (i.e., higher values of f_{PAH}) than those at higher latitudes, as would be expected from PAH destruction in diffuse regions. Again, however, there is no indication of a correlation of the AME intensity per $\mathcal{R}$ with f_{PAH}.

We next examine in Figure 8(c) only those pixels in which one or both of the AME components are significant at greater than 5σ. The cut on AME significance does not change significantly the behavior observed in Figure 8(a) other than to eliminate some pixels with low f_{PAH} values. As illustrated in Figure 4, the pixels with low f_{PAH} also tend to have low surface brightness, which may be responsible for inducing the slight negative correlation observed. Finally, Figure 8(d) shows for comparison the same analysis performed on the standard mask (Figure 3(a)).

The non-correlation of the AME intensity and f_{PAH} is therefore robust to assumptions either on the AME significance or the region of the sky analyzed. We now turn to the implications of this result in the following section.

5. DISCUSSION

One of the largest sources of uncertainty in this analysis is the fidelity of the AME spectrum recovered from decomposition. Due to a lack of data between the *WMAP* 23 GHz band and the Haslam data at 408 MHz, it is difficult to constrain the relative contributions of the AME, synchrotron, and free–free emission in the frequency range of interest. The Planck Collaboration et al. (2015b) note that their estimates of synchrotron emission are lower than the 9-year *WMAP* analysis (Bennett et al. 2013) by about 70% at high Galactic latitudes and factors of several in the Galactic plane, with the AME component estimate being larger as a result. It is therefore possible that the AME map has a non-negligible synchrotron component.

The presence of contamination in the AME map, such as free–free or synchrotron, would of course mean that f_{PAH} is not related to the inferred AME intensity in a perfectly linear way even if the AME comes from spinning PAHs. Further, since f_{PAH} correlates with τ_{353} and $\mathcal{R}$, it is also expected to correlate with the free–free and synchrotron emission, which increase with increasing gas (and therefore dust) column density.

As illustrated in Figure 9(a), $I_\nu^{AME}/\alpha\mathcal{R}$ is weakly anti-correlated with the 30 GHz free–free emission per $\mathcal{R}$ ($r_s = -0.07$).

In Figure 9(b), we plot $I_\nu^{AME}/\alpha\mathcal{R}$ against the 30 GHz synchrotron intensity per $\mathcal{R}$. The two quantities show evidence of a weak positive correlation ($r_s = 0.11$).

In Figure 9(c), we plot $I_\nu^{AME}/\alpha\mathcal{R}$ against the CO(1–0) line intensity per $\mathcal{R}$. The two quantities show possible evidence of a weak positive correlation ($r_s = 0.05$).

It is likely that some degree of contamination from other low-frequency components exists in the AME maps. This is to be expected given the theoretical difficulties modeling their spectra and the relative lack of observational constraints at very low frequencies. In the future, more detailed decomposition enabled by additional data will improve the fidelity of the inferred AME spectrum and test the conclusions derived here. We note that the observed correlations between the AME/$\mathcal{R}$ and the other low-frequency components are rather weak, making it unlikely that these components are driving the observed non-correlation between the AME and f_{PAH}.

Even assuming no contamination in the fit AME component, correlations with the synchrotron emission are plausible. For instance, if the AME arises from spinning ultrasmall grains, it might be affected in synchrotron-bright supernova remnants where it may be enhanced if shattering in grain–grain collisions increases the ultrasmall grain population, or suppressed if ultrasmall grains are destroyed by sputtering.

The theoretical uncertainties in the models for these emission components underscore the need for obtaining ancillary data at lower frequency. Upcoming 5 GHz observations from the C-band All-sky Survey (C-BASS) (King et al. 2014) and 2.3 GHz observations from the S-band Polarized All-sky Survey (S-PASS) (Carretti et al. 2009) will play an invaluable role in disentangling the low-frequency components.

A second source of uncertainty is the ability of $f_{PAH} \equiv \Delta(\nu I_\nu)^{12\,\mu m}/\Delta\mathcal{R}$ to trace the PAH abundance. In particular, the fraction of the PAH emission appearing in the *WISE* 12 μm band can depend on the ionization state of the PAHs and other properties of the local environment (e.g., Draine & Li 2007; Draine 2011). Thus it may be possible to "wash out" a correlation between f_{PAH} and the AME intensity even if the AME arises from spinning PAHs.

To test the plausibility of such a scenario, in Figure 10 we correlate the AME intensity per $\mathcal{R}$ with f_{PAH} only in pixels with similar environmental conditions as determined by their fit dust temperature and β. We find no significant differences from our primary analysis and thus no evidence that variations in the local environment are driving the lack of correlation between f_{PAH} and the AME intensity per $\mathcal{R}$.

In addition to the uncertainties discussed above, each observable A also has an associated observational uncertainty σ_A which we have not included in Equation (3). σ_A is highly degenerate with σ_α and thus it is difficult to quantify their relative contributions to the total uncertainty. Instead, we ask what assumed fractional uncertainty on A would be required for the data to be consistent with an intrinsic relationship with $\sigma_\alpha/\alpha = 0.2$, comparably tight as found with $\mathcal{R}$. We denote this quantity $\sigma_A/A\,(0.2)$ in Table 1, finding that for τ_{353} and $f_{PAH}\tau_{353}$, σ_A/A would need to be larger than 25% for the observations to be consistent with an intrinsic relationship with so narrow a dispersion. The small uncertainties on the thermal dust emission at 353 GHz reported by the Planck Collaboration et al. (2015b) are inconsistent with what would be required for the data to be compatible with a tight intrinsic relationship between AME and either τ_{353} or $f_{PAH}\tau_{353}$. Thus, it does not
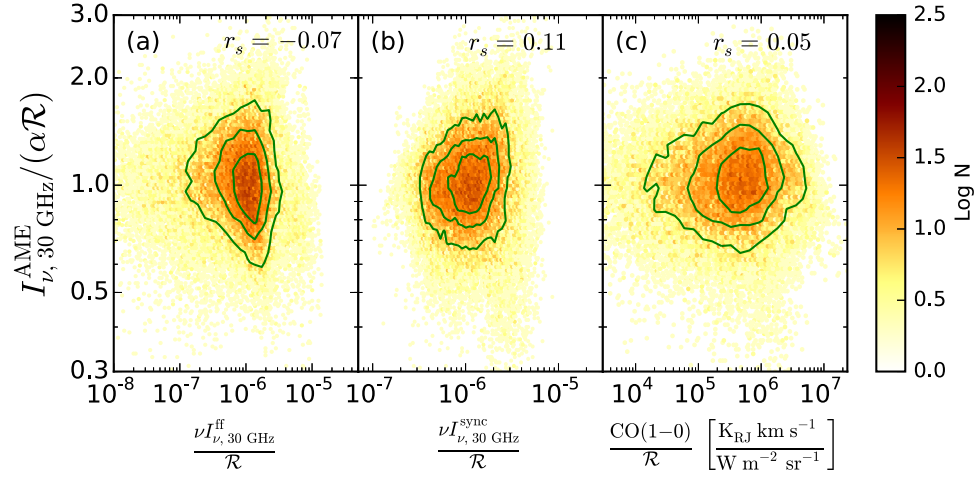
Figure 9. 30 GHz AME intensity normalized by $\alpha\mathcal{R}$ is plotted against (a) the 30 GHz free–free intensity, (b) the 30 GHz synchrotron intensity, and (c) the CO(1–0) line emission all normalized by $\mathcal{R}$. There is evidence for weak correlation in all panels.
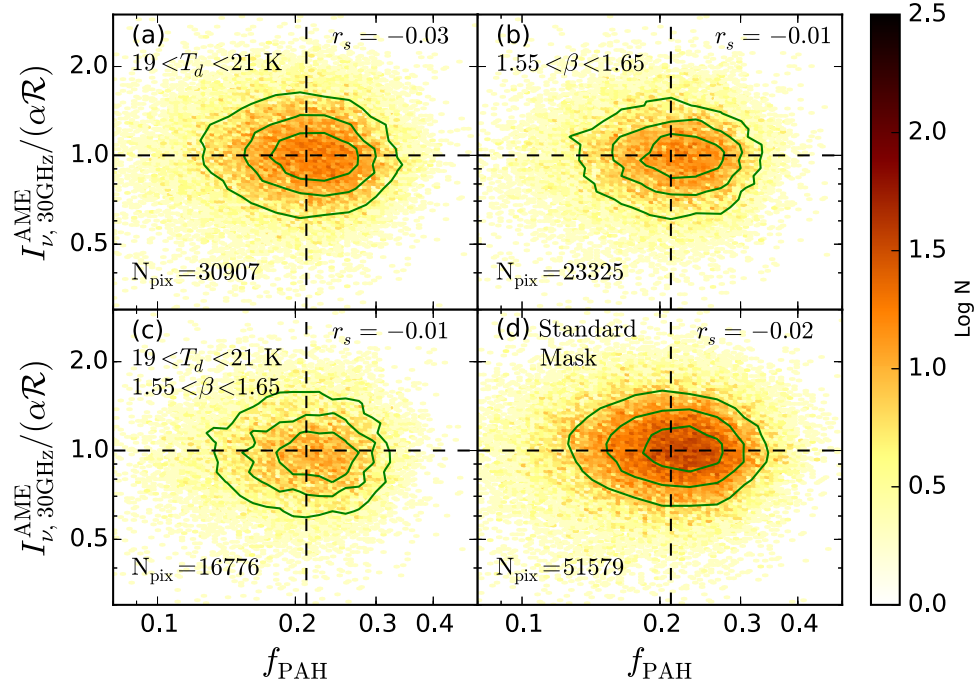

Figure 10. As in Figure 8, f_{PAH} is plotted against the 30 GHz AME intensity normalized by $\alpha\mathcal{R}$. We examine four different sets of pixels: (a) pixels with T_d between 19 and 21 K (typical of the high-latitude sky), (b) pixels with β between 1.55 and 1.65, (c) pixels meeting both the criteria of panels (a) and (b), and (d) using the standard mask only. For reference, the dashed lines mark the median values in the standard mask. Thus even when the conditions of the local environment are held relatively fixed, there is no evidence for a positive correlation between the AME and f_{PAH}.

seem plausible to attribute the entirety of our findings to the relative uncertainties of the observables.

Finally, the Planck Collaboration et al. (2015c) demonstrate that the correlation between AME/$\mathcal{R}$ and f_{PAH} can be affected by systematic errors in the determination of $\mathcal{R}$. Although an analysis using the Commander-derived $\mathcal{R}$ and f_{PAH} determined by straight division of the W3 and $\mathcal{R}$ maps is inappropriate for the reasons discussed in Section 2.3, it remains possible that the $\mathcal{R}$ map produced by the Planck Collaboration et al. (2014a) is biased in ways that affect the correlation with f_{PAH}. Dust modeling employing additional data, such as 60 μm dust emission, will help clarify this issue. In the meantime, we note that $\mathcal{R}$, being the integral of the FIR dust intensity, is rather insensitive to the specifics of modeling

as long as the model provides a reasonable fit to the data. Thus, particularly when 100 μm data are employed, $\mathcal{R}$ is straightforward to determine and we have no reason to suspect strong systematic biases.

If indeed the AME is *not* correlated with the PAH abundance and *is* correlated with the strength of the radiation field, what are the implications for the origin of the emission? We present two possibilities:

1. The AME is spinning dust emission that arises primarily from ultrasmall grains that are not PAHs. Li & Draine (2001) have shown that as much as ~10% of the interstellar silicate mass could be in ultrasmall grains. However, it remains to be seen whether these grains

could produce enough rotational emission to account for the AME.

2. The AME is predominantly thermal dust emission, such as magnetic dipole emission from magnetic materials. However, the relationship between AME/$\mathcal{R}$ and T_d does not appear consistent with thermal emission (see Figure 5). Additionally, current models of magnetic dipole emission do not predict behavior that could emulate the observed AME SED without invoking highly elongated (e.g., 5:1 prolate spheroids) Fe inclusions (Draine & Hensley 2013). Furthermore, thermal dust emission from an aligned component of the grain population is expected to be significantly polarized, including magnetic dipole emission from ferromagnetic inclusions (Draine & Hensley 2013), at odds with current non-detections of AME polarization. Nevertheless, the theoretical calculations of the emissivities of these magnetic materials are still quite uncertain, and more laboratory data are needed to assess the behavior of magnetic materials at microwave frequencies to determine whether such grains could be a potential source of the AME. It remains conceivable that some interstellar grain component might produce the AME by non-rotational electric dipole radiation, but we are not aware of materials that could do this.

Invoking an alternative explanation for the AME also requires explaining why the PAHs are *not* a substantial source of spinning dust emission. Because the PAHs are clearly present and must be rotating, this would require that the electric dipole moments of the PAHs have been significantly over-estimated (the spinning dust emission scales as the square of the dipole moment). The electric dipole moments of selected hydrocarbon molecules compiled by Draine & Lazarian (1998b) have a scatter of nearly an order of magnitude. Further, harsh UV irradiation more easily destroys asymmetric molecules, perhaps preferentially selecting for a population of more symmetric PAHs with smaller dipole moments. Thus it is plausible that the dipole moment distributions adopted in spinning dust models may significantly overestimate the true electric dipole moments of interstellar PAHs.

Lazarian & Draine (2000) estimated the polarization fraction of spinning dust emission to be $p \lesssim 0.01$ near 30 GHz. This estimate would also apply to spinning dust emission from non-PAH grains. However, if the AME is thermal emission from large aligned grains, it should be significantly polarized with $\boldsymbol{E} \perp \boldsymbol{B}_0$ for electric dipole radiation or $\boldsymbol{E} \| \boldsymbol{B}_0$ for magnetic dipole radiation from magnetic inclusions (Draine & Hensley 2013).

Observations of known AME sources in polarization suggest minimal polarization of the AME. In the Perseus molecular cloud, the polarization fraction of the total emission was found to be $3.4^{+1.5}_{-1.9}\%$ at 11 GHz (Battistelli et al. 2006), less than 6.3% at 12 GHz (Génova-Santos et al. 2015), less than 2.8% at 18 GHz (Génova-Santos et al. 2015), and less than ~1% at 23 GHz (Dickinson et al. 2011; López-Caraballo et al. 2011). Likewise, observations of the ρ Ophiuchi molecular cloud have yielded upper limits of $\lesssim 1\%$ at 30 GHz (Casassus et al. 2008; Dickinson et al. 2011). Mason et al. (2009) placed an upper limit of 2.7% on the 9.65 GHz polarization fraction in the dark cloud Lynds 1622. 21.5 GHz observations of the H II region RCW175 yielded a polarization fraction of $2.2 \pm 0.4\%$ (Battistelli et al. 2015), although it is unclear whether this

polarization is arising from the AME or a sub-dominant synchrotron component.

These upper limits on polarization in the 10–30 GHz emission appear to favor spinning dust emission from a non-PAH population of ultrasmall grains.

6. CONCLUSION

We have combined the *Planck* foreground component maps, *Planck* modified blackbody dust parameter maps, and *WISE* 12 μm maps to test key predictions of the spinning PAH hypothesis. The principal conclusions of this work are as follows:

1. τ_{353}, the dust radiance $\mathcal{R}$, and $I_\nu^{12\,\mu m}$ are all excellent predictors of the 30 GHz AME intensity. $\mathcal{R}$ exhibits the tightest correlation, suggesting that the AME is sensitive to the strength of the radiation field.
2. Neither AME/τ_{353} nor AME/$\mathcal{R}$ show any correlation with the PAH emission whether considering the full sky, regions close to the Galactic plane, or higher Galactic latitudes.
3. We find that f_{PAH} is correlated with both τ_{353} and $\mathcal{R}$, consistent with PAH destruction in low density regions.
4. Taken together, these facts pose a serious challenge to the spinning PAH paradigm as the explanation for the AME. Alternative explanations, such as magnetic dipole emission from ferro- or ferrimagnetic grains, should be more thoroughly investigated.
5. More low-frequency constraints are needed to break degeneracies between the AME, free–free, and synchrotron emissions to enable more accurate decomposition and to better constrain the AME spectrum. Upcoming all-sky observations from C-BASS and S-PASS will thus facilitate deeper investigations into the origin of the AME.
6. Further measurements of AME polarization will help clarify the nature of the grains responsible for the AME.

REFERENCES

Ali-Haïmoud, Y., Hirata, C. M., & Dickinson, C. 2009, MNRAS, 395, 1055
Alves, M. I. R., Davies, R. D., Dickinson, C., et al. 2010, MNRAS, 405, 1654
Battistelli, E. S., Carretti, E., Cruciani, A., et al. 2015, ApJ, 801, 111
Battistelli, E. S., Rebolo, R., Rubiño-Martín, J. A., et al. 2006, ApJL, 645, L141
Bennett, C. L., Larson, D., Weiland, J. L., et al. 2013, ApJS, 208, 20
Carretti, E., Gaensler, B., Staveley-Smith, L., et al. 2009, S-band Polarization All Sky Survey (S-PASS), ATNF Proposal
Casassus, S., Cabrera, G. F., Förster, F., et al. 2006, ApJ, 639, 951
Casassus, S., Dickinson, C., Cleary, K., et al. 2008, MNRAS, 391, 1075
Davies, R. D., Dickinson, C., Banday, A. J., et al. 2006, MNRAS, 370, 1125

de Oliveira-Costa, A., Kogut, A., Devlin, M. J., et al. 1997, ApJL, 482, L17
Dickinson, C., Peel, M., & Vidal, M. 2011, MNRAS, 418, L35
Dobler, G., Draine, B., & Finkbeiner, D. P. 2009, ApJ, 699, 1374
Dong, R., & Draine, B. T. 2011, ApJ, 727, 35
Draine, B. T. 2011, in EAS Publications Ser. 46, PAHs and the Universe: A Symposium to Celebrate the 25th Anniversary of the PAH Hypothesis, ed. C. Joblin & A. G. G. M. Tielens (Princeton, NJ: Princeton Univ. Press), 29
Draine, B. T., & Hensley, B. 2013, ApJ, 765, 159
Draine, B. T., & Lazarian, A. 1998a, ApJL, 494, L19
Draine, B. T., & Lazarian, A. 1998b, ApJ, 508, 157
Draine, B. T., & Lazarian, A. 1999, ApJ, 512, 740
Draine, B. T., & Li, A. 2007, ApJ, 657, 810
Eriksen, H. K., Dickinson, C., Lawrence, C. R., et al. 2006, ApJ, 641, 665
Eriksen, H. K., Jewell, J. B., Dickinson, C., et al. 2008, ApJ, 676, 10
Eriksen, H. K., O'Dwyer, I. J., Jewell, J. B., et al. 2004, ApJS, 155, 227
Foreman-Mackey, D., Hogg, D. W., Lang, D., & Goodman, J. 2013, PASP, 125, 306
Génova-Santos, R., Martín, J. A. R., Rebolo, R., et al. 2015, MNRAS, 452, 4169
Górski, K. M., Hivon, E., Banday, A. J., et al. 2005, ApJ, 622, 759
Haslam, C. G. T., Salter, C. J., Stoffel, H., & Wilson, W. E. 1982, A&AS, 47, 1
Hensley, B., Murphy, E., & Staguhn, J. 2015, MNRAS, 449, 809
Hoang, T., Draine, B. T., & Lazarian, A. 2010, ApJ, 715, 1462
Hoang, T., Lazarian, A., & Draine, B. T. 2011, ApJ, 741, 87
Hogg, D. W., Bovy, J., & Lang, D. 2010, arXiv:1008.4686
King, O. G., Jones, M. E., Blackhurst, E. J., et al. 2014, MNRAS, 438, 2426
Kogut, A., Banday, A. J., Bennett, C. L., et al. 1996, ApJ, 460, 1
Lazarian, A., & Draine, B. T. 2000, ApJL, 536, L15
Leitch, E. M., Readhead, A. C. S., Pearson, T. J., & Myers, S. T. 1997, ApJL, 486, L23
Li, A., & Draine, B. T. 2001, ApJL, 550, L213
López-Caraballo, C. H., Rubiño-Martín, J. A., Rebolo, R., & Génova-Santos, R. 2011, ApJ, 729, 25

Mason, B. S., Robishaw, T., Heiles, C., Finkbeiner, D., & Dickinson, C. 2009, ApJ, 697, 1187
Meisner, A. M., & Finkbeiner, D. P. 2014, ApJ, 781, 5
Meisner, A. M., & Finkbeiner, D. P. 2015, ApJ, 798, 88
Miville-Deschênes, M.-A., & Lagache, G. 2005, ApJS, 157, 302
Miville-Deschênes, M.-A., Ysard, N., Lavabre, A., et al. 2008, A&A, 490, 1093
Murphy, E. J., Helou, G., Condon, J. J., et al. 2010, ApJL, 709, L108
Planck Collaboration, Abergel, A., Ade, P. A. R., et al. 2014a, A&A, 571, A11
Planck Collaboration, Abergel, A., Ade, P. A. R., et al. 2014b, A&A, 566, A55
Planck Collaboration, Adam, R., Ade, P. A. R., et al. 2015a, arXiv:1502.01582
Planck Collaboration, Adam, R., Ade, P. A. R., et al. 2015b, arXiv:1502.01588
Planck Collaboration, Ade, P. A. R., Aghanim, N., et al. 2014c, A&A, 565, A103
Planck Collaboration, Ade, P. A. R., Aghanim, N., et al. 2014d, A&A, 586, A132
Planck Collaboration, Ade, P. A. R., Aghanim, N., et al. 2015c, arXiv:1506.06660
Scaife, A. M. M., Nikolic, B., Green, D. A., et al. 2010, MNRAS, 406, L45
Schlegel, D. J., Finkbeiner, D. P., & Davis, M. 1998, ApJ, 500, 525
Silsbee, K., Ali-Haïmoud, Y., & Hirata, C. M. 2011, MNRAS, 411, 2750
Su, M., Slatyer, T. R., & Finkbeiner, D. P. 2010, ApJ, 724, 1044
Tibbs, C. T., Flagey, N., Paladini, R., et al. 2011, MNRAS, 418, 1889
Tibbs, C. T., Paladini, R., Compiègne, M., et al. 2012a, ApJ, 754, 94
Tibbs, C. T., Paladini, R., & Dickinson, C. 2012b, AdAst, 2012, 41
Tibbs, C. T., Watson, R. A., Dickinson, C., et al. 2010, MNRAS, 402, 1969
Todorović, M., Davies, R. D., Dickinson, C., et al. 2010, MNRAS, 406, 1629
Wheelock, S. L., Gautier, T. N., Chillemi, J., et al. 1994, STIN, 95, 22539
Wright, E. L., Eisenhardt, P. R. M., Mainzer, A. K., et al. 2010, AJ, 140, 1868
Ysard, N., Miville-Deschênes, M. A., & Verstraete, L. 2010, A&A, 509, L1
Ysard, N., & Verstraete, L. 2010, A&A, 509, A12